Available online at www.sciencedirect.com
ScienceDirect
Journal of Computational Physics 227 (2008) 9216–9240
JOURNAL OF COMPUTATIONAL PHYSICS
www.elsevier.com/locate/jcp

Vortex particle methods in aeroacoustic calculations

Serge Huberson [a], Elie Rivoalen [b,*], Spyros Voutsinas [c]

[a] Université de Poitiers, Laboratoire d'Etudes Aérodynamiques, Boulevard Marie et Pierre Curie BP 30179, 86962 Futuroscope Chasseneuil Cedex, France
[b] Université du Havre, Laboratoire Ondes et Milieux Complexes, 53 rue de Prony B.P. 540, 76058 Le Havre Cedex, France
[c] National Technical University of Athens, School of Mechanical Engineering, 9 Heroon Polytechniou Str, 15773 Athens, Greece

Received 17 June 2007; received in revised form 8 May 2008; accepted 5 June 2008
Available online 25 June 2008

Abstract

The connection between vortex particle methods and aeroacoustics is considered within the framework of Lighthill's acoustic analogy which allows to decouple the flow from noise propagation. For the flow, techniques such as tree-algorithms and the particle-mesh method are brought together with the aim to achieve the best possible performance in view of analyzing complex problems. The flow results are then input to the acoustic wave equation which is solved in integral form. It will involve monopole, dipole and quadrupole terms which can be successively integrated. The significance of such an approach is first demonstrated in two problems, both related to vortex–solid interactions. The first is a generic one and considers the interaction of a vortex filament interacting with a sphere while the second considers helicopter noise as an example of a complex engineering set-up.

Keywords: Vortex sound; Vortex flows; CFD; Acoustic analogy; Helicopter noise

1. Introduction

Aeroacoustic calculations were made possible in the early nineties thanks to the conjugate progress of CFD and computers. About 20 years later, it remains a very challenging problem and the complete modelisation of the acoustical properties of complex flows still relies for a part on empirical modelisation. Within this context, particle methods brought a decisive contribution to CFD and were probably the very first methods able to produce reliable prediction tools in realistic situations. The properties of the particle method have been thoroughly commented since the basic papers by Chorin [1] and Leonard [2] and need not be extensively reviewed here. It suffices to mention their ability to transport vorticity for very long times and distances and the relatively good approximation provided even with coarse discretisations. These are two ingredients of paramount importance in any aeroacoustic simulation. Besides this, the initial drawback of high computing cost was readily overcome by the development of the so-called tree-algorithms [3] and its later combination with

* Corresponding author.
E-mail addresses: serge.huberson@univ-poitiers.fr (S. Huberson), elie.rivoalen@univ-lehavre.fr (E. Rivoalen), spyros@fluid.mech.ntua.gr (S. Voutsinas).

0021-9991/$ - see front matter © 2008 Elsevier Inc. All rights reserved.
doi:10.1016/j.jcp.2008.06.011

cloud-in-cells methods [4,5]. The possibility, thus offered, to use larger number of discretisation points brought into light the fact that the two first-mentioned qualities of vortex methods constituted also the basis for capturing very small vortex structures developing within boundary layers or wakes through instabilities [6]. This ability obviously enforced the initial interest of particle methods for aeroacoustic simulations.

The first question arising with subsonic aeroacoustics concerns the importance of compressibility. Although compressibility is necessary for sound propagation, its role in sound generation is immersed within the pressure fluctuations which depend on a lot of other factors, while the relative importance of these factors itself depends on the flow properties. However, it can be pointed out that a lot of interesting subsonic flows are subjected to the usual splitting between an incompressible generation of pressure fluctuations and a slightly compressible propagation of sound according to Lighthill's acoustic analogy [7]. Therefore, sound prediction can rely on the combination of an incompressible particle calculation and a linear solver for the propagation of the produced sound. In case the account of compressibility cannot be avoided (as in the case of transonic flows), the particle method was also extended by several authors [8,9]. The development of this last method was brought as far as the computation of the noise produced by two interacting vortex rings [10].

An other important aspect of aeroacoustic simulations is the necessity to deal with three-dimensional calculations for realistic configurations. Once again the ability of particle methods to provide a rather good approximation with a reduced number of discretisation points was early recognized and allowed the first three dimensional simulations that actually account for complex vortex systems. The pioneering calculation around fixed wings by Rehbach [11] was rapidly extended to more complex configurations and soon the first calculations around helicopter rotor–fuselage combinations were made possible [12]. Particle methods, like vortex filament methods, transport vorticity, and have to directly deal with stretching effects which introduce non-trivial numerical problems. However, they also allow a direct control of the vortex stretching thus providing a better insight on one of the crucial mechanisms underlying three-dimensional flows.

In this paper, the noise generation by flows envolving vortex–solid interactions is investigated in the context of the vortex particle method. This goal has been reached by using an assemblage of different elements that allow to simulate complex configurations considering that a direct simulation of the whole problem is not affordable by existing computational power but probably also in the near future. The model used is based on the Ffowcs Williams and Hawkings equation whose properties are briefly recalled in Section 2.1. For the flow the vortex method is applied to unsteady inviscid three-dimensional flows involving solid boundaries. This well-known method will be shortly described in Section 2.2, as well as the more recent improvements which eventually made the present calculations possible.

The method is first applied to the axi-symmetric problem of a vortex tube interacting with a rigid sphere. It is worth noting that it constitutes the simplest flow exhibiting stretching effects which allows to reduce the computational effort to a 2D meridian plane calculation. Therefore, axi-symmetric flows were found to provide a valuable test-case for later full three-dimensional calculations. Because of the simplification expected in this particular configuration, it is possible to significantly increase the number of particles used in describing the flow within the tube section as compared to an actual three-dimensional simulation. However, the equation to be solved, although derived from the three-dimensional vorticity transport equation, is significantly different and therefore a particular solution procedure has to be used. All these points will be described in Section 3.

Then in order to show that the same set-up can be successfully used in complex problems of significant engineering interest, the case of helicopter noise is considered in Section 4. It is a quite rich problem since vorticity is fed continuously in the wake of the main rotor which because of its positioning in extreme yaw, renders the wake evolution and in particular its interaction with the blades (blade–vortex-interaction) critical for noise predictions and noise control. Moreover in many flight conditions, the main rotor wake will impinge the tail rotor which again represents a significant noise producing mechanism.

2. Noise predictions in practice using vortex methods

2.1. Noise modelling

Theoretically, noise-flow decoupling is justified in the context of linear aeroacoustics which originates from Lighthill's pioneering work on acoustic analogy. The general case involves the sound generated by a moving

and possibly deformable body. This case was initially considered by Ffowcs Williams and Hawkings [13], giving as main result the famous FW–H equation (see also [14]):

$$\frac{\partial^2\rho'}{\partial t^2} - c^2\nabla\rho' = \frac{\partial}{\partial t}[Q\delta(S)] + \frac{\partial}{\partial x_i}[F_i\delta(S)] + \frac{\partial}{\partial x_i\partial x_j}[T_{ij}H(S)] \tag{1}$$

where

$$Q = [\rho_o V_i + \rho(u_i - V_i)]\frac{\partial S}{\partial x_i} \tag{2}$$

$$F_i = -[p\delta_{ij} + \tau_{ij} + \rho u_i(u_j - V_j)]\frac{\partial S}{\partial x_j} \tag{3}$$

$$T_{ij} = \{\rho u_i u_j + [p - p_o - c^2(\rho - \rho_o)]\delta_{ij} - \tau_{ij}\} \tag{4}$$

c is the speed of sound, ρ' denotes the acoustic density perturbation, S denotes the surface containing the sources moving with velocity $\mathbf{V}$, ρ_o and p_o denote the fluid density and pressure at rest, $\delta(S), H(S)$ denote the surface Dirac and Heaviside functions, respectively, u_i denotes the fluid velocity, τ_{ij} denotes the viscous stress tensor and T_{ij} Lighthill's tensor. In this form FW–H equation represents another way of writing the exact flow equations and therefore it is not useful since the source terms depend on the acoustic field. Following Lighthill's idea of acoustic analogy, the problem can be reduced into a classical acoustic radiation one for given sources. To this end, the right hand side is simplified by assuming that all information required is provided by the flow solver. So instead of solving the complete flow equations, we aim at appropriately defining the sound sources. This interpretation of the FW–H equation was used subsequently by Farassat and coworkers [15] who derived a variety of formulations for the acoustic pressure in closed form. In (1), already the three types of sound sources can be identified: the monopoles, the dipoles and the quadrupoles named after their directivity pattern and appearing in this sequence. Monopoles (thickness term) are generated by the unsteady motion of the solid boundaries, dipoles are generated by surface loading (loading term) and quadrupoles are generated by Lighthill's stress tensor which contains the contribution of the spatially distributed vorticity, the compressive stress tensor and the density variations.

Calculation of the quadrupole noise term represents a major task because it involves a volume integral. That is why in practice quadrupoles are retained only when necessary. A valuable remark made recently by Di Francescantonio [16] allows bypassing the computation of the quadrupole term, provided that the noise sources are compactly defined in space. Measurements have shown that the quadrupole term is important in the vicinity of the solid surfaces, so the idea is to introduce a permeable surface S containing all (or the most important) quadrupole sources and compute noise outside of it. This means that monopole and dipole noise source distributions are no longer needed on the solid surfaces but over this artificial surface.

2.2. Description of the flow model

For the flow, the baseline solver uses Hess's panel method in order to account for the presence of the solid boundaries [17] which is combined with a vortex particle approximation of the wake [18]. Solid components can be either non-lifting or lifting in which case they generate surface vortex wakes. Source distributions σ are defined over all solid boundaries while dipole distributions μ are added on lifting bodies, and their wakes. Under these assumptions the perturbation flow velocity $\mathbf{u}_{\text{solid}} = \nabla\phi$ takes the form:

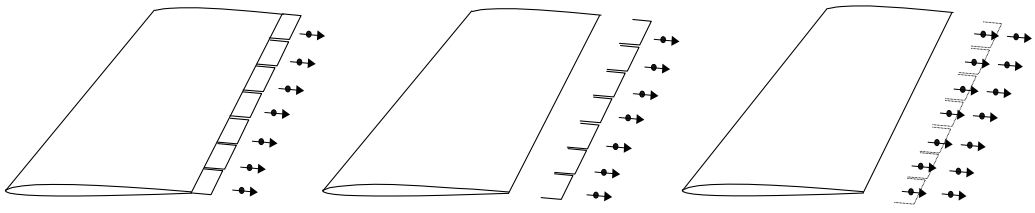

Fig. 1. The generation of vortex particles along the trailing edge of a wing within a time step.

$$-\phi(\mathbf{x},t)=\int_{S_B}\left(\frac{\sigma(\mathbf{y},t)}{4\pi r}-\frac{\mu(\mathbf{y},t)(\mathbf{n}\cdot\mathbf{r})}{4\pi r^3}\right)\mathrm{d}S-\int_{S_W}\frac{\mu_W(\mathbf{y},t)(\mathbf{n}_W.\mathbf{r})}{4\pi r^3}\,\mathrm{d}S \tag{5}$$

where S_B denotes collectively the solid boundaries which are considered moving with velocity $\mathbf{V}$, S_W the surface wakes, $\mathbf{r}=\mathbf{x}-\mathbf{y}$ and $\mathbf{n}$ denotes the normal to either surface. The no-penetration condition applied on S for the total flow velocity: $\mathbf{u}:(\mathbf{u}-\mathbf{V})\mathbf{n}=0$ can determine σ while for μ and μ_W we make use of Kelvin's theorem. At any point $\mathbf{y}\in S_W$, the circulation of any closed circuit cutting S_W at $\mathbf{y}$ only, is equal to $-\mu_W$ so if the circulation is materially conserved then μ_W will retain at all times the value it took at the time it was released from the solid boundary into the free flow. The wake generation process takes place along the so called emission lines which in the case of a blade will contain the trailing edge but can be extended over the tips as done here in view of generating a concise tip vortex. So from the history of the flow μ_W is everywhere known except along the emission lines where $\mu\equiv\mu_W$. Then for μ, the Kutta condition imposing zero pressure jump along the emission line is applied. This means that in the case of a blade, the variation of μ is constrained only along the span, while its chordwise variation is a matter of choice. Following Hess, it is assumed that μ varies linearly with the length along each blade section.

The passage to the interpretation of the wakes as regions carrying vorticity, is realised following Hess's remark that the flow induced by a dipole surface distribution μ defined on a surface S, is equivalent to a surface term involving surface vorticity $\boldsymbol{\gamma}=\mathbf{n}\times\nabla\mu$ and a line vortex term over the boundary of S, ∂S:

$$\mathbf{u}_\mu(\mathbf{x})=\int_S\frac{\boldsymbol{\gamma}(\mathbf{y})\times\mathbf{r}}{4\pi r^3}\,\mathrm{d}S+\oint_{\partial S}\frac{\mu(\mathbf{y})\mathrm{d}\ell\times\mathbf{r}}{4\pi r^3} \tag{6}$$

By integrating surface and line vorticity in the wake, a collection of vortex particles is obtained. In practice this is needed only for the part of the wake generated within the current time step as indicated in Fig. 1. This approximation results in a vorticity field $\boldsymbol{\omega}$ defined by the strengths $\boldsymbol{\Omega}_p(t)$ being products of vorticity and volume, and the positions $\mathbf{Z}_p(t)$ of the vortex particles:

$$\frac{\mathrm{d}\mathbf{Z}_p(t)}{\mathrm{d}t}=\mathbf{u}(\mathbf{Z}_p,t),\quad \frac{\mathrm{d}\boldsymbol{\Omega}_p(t)}{\mathrm{d}t}=(\boldsymbol{\Omega}(t)\cdot\nabla)\mathbf{u}(\mathbf{Z}_p,t) \tag{7}$$

In Eq. (7), $\mathbf{u}$ will be given as the sum of the velocity at infinity $\mathbf{u}_\infty$, $\mathbf{u}_{\text{solid}}$ as defined in (5) but with S_W covering only the wake strip generated at the current step, and $\mathbf{u}_\omega$:

$$\mathbf{u}_\omega(\mathbf{x},t)=\sum_p\frac{\boldsymbol{\Omega}_p(t)\times(\mathbf{x}-\mathbf{Z}_p(t))}{4\pi|\mathbf{x}-\mathbf{Z}_p(t)|^3}f_\epsilon(\mathbf{x}-\mathbf{Z}_p) \tag{8}$$

where f_ϵ denotes the cut-off function introduced in order to regularize the flow. Note that the above equation can be directly differentiated in order to determine the deformation term in (7).

The above formulation can be translated into a time marching scheme as follows: first solve the integral equation corresponding to the no-penetration condition together with the Kutta condition along the emission line and determine the source and dipole distributions. This corresponds to the potential calculations. They depend on the geometry of the wake generated during the actual time step. So iterations are needed until the geometry of the wake converges. Typically, 3–4 iterations are enough provided that the size of the wake panels are comparable to those on the solid boundary. Given the wake geometry and μ_W, integration provides the strengths and locations of the new vortex particles. Finally, all vortex particles are transported by solving (7).

3. Axi-symmetric investigation of the wall/vortex interaction

The most severe helicopter blade–vortex interaction noise (BVI) can be predicted by means of simple 2D modelling provided that the correct wake vortex location relatively to the blade is set [19]. This location can be obtained either from experimental data or as a result of a coarse-mesh 3D calculation. The interaction mechanism is then reduced to a pressure variation which can be used directly as input to a noise-propagation code. Although first order effects have been actually reproduced, further investigation is necessary to assess the capability of the method to account for such effects as noise induced by the vortex inner core fluctuations or

the modification due to curvature effects of the walls and the vortex tubes. Clearly, the frequency of the pressure variations induced by the first effect is irrelevant to BVI which usually involves lower frequencies. However, noise modulation at higher frequencies can also appear to be of some importance which is our motivation for studying the wall/ vortex interaction problem on the simplified configuration of an axi-symmetric vortex filament without swirl, interacting with a sphere. As already mentioned, this case has been selected as the simplest 3D configuration involving stretching.

The two previous effects have been characterized using two dimensionless parameters: the slenderness parameter which is the ratio of the vortex tube sectional diameter σ over the mean curvature radius of the tube R at the beginning of the calculation, and a closeness parameter which characterizes the distance between the sphere and the vortex tube. Actually, the closeness parameter is not directly accessible because it results from the flow calculation. Hereafter, it is assumed that it is a monotonic function of the ratio of the sphere radius a over the vortex tube initial mean radius R. Any calculation will be entirely defined by these two parameters.

3.1. Computational details

3.1.1. The flow model

In this subsection, we focus our attention on axi-symmetric flow fields associated with compact vorticity distribution in the limit of low Mach number and high Reynolds number. We consider the passage of a vortex ring approaching a rigid sphere. This is the same numerical setting used by Knio et al. [20] and Klein et al. [21] to analyse the dynamics and the far field sound of a slender vortex ring approaching a sphere. The essential difference between the two models is that our vortex particle model takes into account the sound generation by the deformation of the vortex core. This point is crucial for acoustics as the ring core radius becomes small [22]. The evolution of the flow field is described in terms of a vorticity-based formulation of the mass and momentum conservation equations in a meridional plane. Thus, we are interested in solutions of the inviscid vorticity transport equation, as expressed in its Lagrangian conservation form:

$$\frac{\mathrm{d}}{\mathrm{d}t}\left(\frac{\omega_\theta}{r}\right) = 0 \tag{9}$$

where ω_θ is the azimuthal component of the vorticity, r is the radial coordinate, t is time and $\mathrm{d}/\mathrm{d}t$ is the material derivative. The velocity field is related to the vorticity by means of the stream function, ψ_θ:

$$\Delta\psi_\theta = -r\omega_\theta \tag{10}$$

$$\mathbf{U} = (u_r, u_z) = \frac{1}{r}\left(-\frac{\mathrm{d}\psi_\theta}{\mathrm{d}z}, \frac{\mathrm{d}\psi_\theta}{\mathrm{d}r}\right) \tag{11}$$

where Δ is the Laplacian operator, z is the axial coordinate and $\mathbf{U} \equiv (u_r, u_z)$ is the velocity vector.

Solid walls modelisation has been described in Section 2.2 and results in an integral equation which have to be solved. Hereafter, the restriction to axi-symmetric flow allows a simplified representation of the walls through images of the vortex elements present within the flow field. In the particular case of a sphere, one can immediately apply the classical result for the image of a coaxial vortex ring [23].

The velocity field is obtained by direct convolution over the field of the particles. Since each Lagrangian particle represents the intersection of a circular filament with the meridional plane, the well-known integral solution of the above stream function Poisson equation (Ref. [23]) can be used. Specifically, a vortex particle having unit circulation and located at $(r_\mathrm{o}, z_\mathrm{o})$ generates a stream function distribution given by

$$\psi_\theta(r, z; r_\mathrm{o}, z_\mathrm{o}) = \frac{1}{4\pi}\int_0^{2\pi} \frac{r r_\mathrm{o}\cos\theta}{\rho}\,\mathrm{d}\theta \tag{12}$$

where $\rho^2 \equiv (z - z_\mathrm{o})^2 + r^2 + r_\mathrm{o}^2 - 2rr_\mathrm{o}\cos\theta$. This expression is singular for $\rho = 0$ and a de-singularisation is necessary, as usual in particle methods. We rely on the regularization scheme introduced by Nitsche and Krasny [24], which replaces the above singular form with:

$$\psi_{\theta\epsilon}(r, z; r_\mathrm{o}, z_\mathrm{o}) = \frac{1}{2\pi}(\rho_1 + \rho_2)(F(\lambda) - E(\lambda)) \tag{13}$$

where ϵ is the regularization parameter,

$$\rho_1^2 \equiv (z-z_o)^2 + (r-r_o)^2 + \epsilon^2, \quad \rho_2^2 \equiv (z-z_o)^2 + (r+r_o)^2 + \epsilon^2$$
$$\lambda \equiv \frac{\rho_2 - \rho_1}{\rho_2 + \rho_1}$$

while F and E, respectively, denote the elliptic functions of the first and second kind. The regularized velocity field, $\mathbf{U}_\epsilon$, is obtained by analytically differentiating Eq. (13).

In the implementation of the particle scheme (Ref. [25]), the vorticity field is represented using a collection of regularized elements. The locations and strengths of the elements are respectively denoted by (r_i, z_i), and Γ_i, where N is the total number of elements. Thus, the evolution of the flow is determined by integrating the following system:

$$\frac{\mathrm{d}\Gamma_i}{\mathrm{d}t} = 0 \tag{14}$$

$$\frac{\mathrm{d}r_i}{\mathrm{d}t} = \sum_{j=1}^{N} u_{er}(r_i, z_i; r_j, z_j) \tag{15}$$

$$\frac{\mathrm{d}z_i}{\mathrm{d}t} = \sum_{j=1}^{N} u_{ez}(r_i, z_i; r_j, z_j) \tag{16}$$

with

$$u_{er}(r, z; r_j, z_j) = -\frac{\Gamma_j}{r_j}\frac{\mathrm{d}\psi_\theta}{\mathrm{d}z}(r, z; r_j, z_j) \tag{17}$$

$$u_{ez}(r, z; r_j, z_j) = \frac{\Gamma_j}{r_j}\frac{\mathrm{d}\psi_\theta}{\mathrm{d}r}(r, z; r_j, z_j) \tag{18}$$

By a simple explicit derivation of the stream function (Eq. (13)), the velocity can be expressed in terms of complete elliptic integral (Refs. [24,25]). Time integration of Eqs. (15) and (16) is performed using fourth order Runge–Kutta scheme.

As mentioned earlier, the particle scheme outlined above is applied to the study of vortex rings interacting with a rigid sphere. The analysis is based on the evaluation of several integral quantities which describe the state of the vortex ring. In particular, the coordinates (R, Z) of the average ring position are defined using:

$$R^2 = \frac{\int_S \omega_\theta r^2 \,\mathrm{d}S}{\int_S \omega_\theta \,\mathrm{d}S} \tag{19}$$

$$Z = \frac{\int_S \omega_\theta r^2 z \,\mathrm{d}S}{\int_S \omega_\theta r^2 \,\mathrm{d}S} \tag{20}$$

where S denotes the support of the vorticity.

3.1.2. The acoustic model

From the far field behaviour of an unsteady 3D vortical flow outside a stationary sphere, the acoustic far field was obtained by Knio et al. [20]. For an axi-symmetric distribution of vorticity that interacted with a rigid sphere, the far field acoustic pressure noise reduced to:

$$p_a^F(\mathbf{x}, t) = \frac{M}{4\mathbf{r}}(D(t_r)/\pi)'' + \frac{M^2}{4\mathbf{r}}(Q(t_r)/(3\pi))''' \tag{21}$$

where $\mathbf{r}$ is the distance location, M is the Mach number and $t_r = t - M\mathbf{r}$ is the retarded time. The pressure far field is governed by the $\mathrm{O}(M)$ dipole D and the $\mathrm{O}(M^2)$ quadrupole Q. In the presence of the sphere the dipole and quadrupole strengths are expressed as

$$D = \pi\cos\theta \int_S \omega_\theta r^2 \left(1 - \left(\frac{a}{x}\right)^3\right)\mathrm{d}S \tag{22}$$

$$Q = 3\pi(\cos^2\theta - 1/3)\int_S \omega_\theta r^2 z \left(1 - \left(\frac{a}{x}\right)^5\right)\mathrm{d}S \tag{23}$$

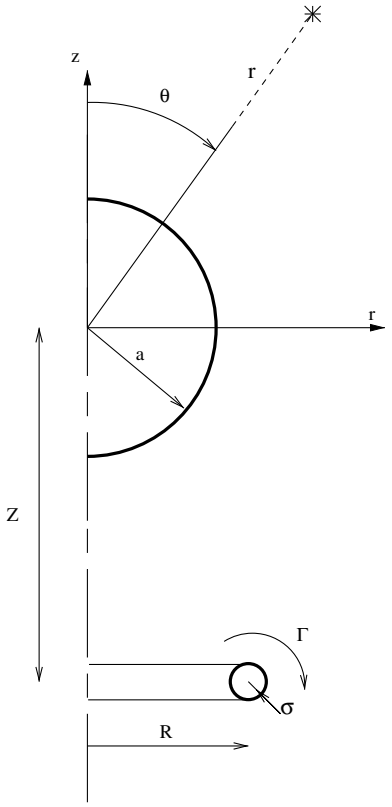

Fig. 2. Schematic illustration of the initial flow configuration in the (r, z) meridian plane.

where $x^2 = r^2 + z^2$, a is the ring radius of the sphere, $M = \Gamma/a/c_0$ is the Mach number and θ is the directivity (cf. Fig. 2). The total circulation of the vortex ring is

$$\Gamma = \int_S \omega_\theta \, \mathrm{d}s$$

and the speed of sound is c_0. In the absence of the sphere the first term of Eq. (21) drops out. The normalized acoustic pressure (Eq. (21)) is obtained as

$$p_{\mathrm{a}}^F = \frac{a^2 \tilde{p}}{\rho_0 \Gamma^2}$$

where ρ_0 is the density.

3.2. Results

Fig. 3 shows the distribution of the particles at different times in the axi-symmetric calculations. For a thin ring with $\sigma/R = 0.1$; in this case the initial ring radius coincides with that of the sphere, $(R/a = 1)$. Also plotted in Fig. 3 is the trajectory of the centroid (Eqs. (19) and (20)) of the core vorticity. The results indicate that as the vortex ring passes over the sphere, its radius stretches while its cross-section becomes thinner [26]. Due to their larger self-induced velocity, thin rings complete the passage in a shorter time period than thicker rings. As the core to radius ratio decreases the trajectory of the core centroid comes closer to the surface of the sphere.

The normalized far-field acoustic pressure for a passage with $\sigma/R = 0.1$, $R/a = 1$ and Mach number $M = 0.05$ is plotted in Fig. 4. Results for acoustic emission along the axis of propagation ($\theta = 0$ and $\theta = 180$) and for emission normal to the ring axis ($\theta = 90$) are given in this Fig. 7. Meanwhile, the acoustic

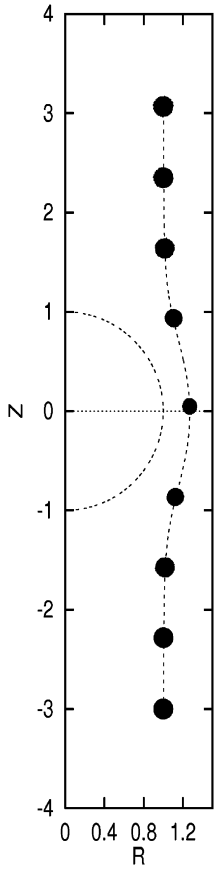

Fig. 3. Position of particles in the core section of vortex ring at different time step. The initial position of vortex ring is $R = 1$ and $Z = -3$ at $t = 0$. The repartition of vorticity is uniform in the section: $\omega_0/r = C$ (Fraenkel section) and the parameter of the section is $\sigma/R = 0.1$. The initial number of particles to describe the section is 841. Only the half plane ($R > 0$) is plotted. The vortex ring travels from the bottom to the top of the figure. The radius of the sphere is $a = 1$ and its position is $Z = 0$ on the axis, the time step it $\Delta t\Gamma/a^2 = 0.0045$. The location of vortex ring in the (R, Z) plane at time $t\Gamma/a^2 = 0$, 4.5, 9, 13.5, 18.

pressure signal computed in the particle simulation reveals a high-frequency component that is not observed in the filament calculations (Refs. [20,26]). In fact, the acoustic signal in the particle simulation appears to be composed of a low-frequency component, whose evolution is in agreement with the signal from a slender vortex model, on which high-frequency oscillations are superimposed [22]. Analysis of the computations indicates that the origin of the high-frequency oscillations is due to unsteady, non-axi-symmetric motion within the vortex core.

Prior to the passage, the unsteady motion has a very small amplitude, since the particle calculations were initialized using the steady, asymptotic, constant-vorticity core distribution given by Fraenkel [27] (labelled FR1 in Table 1). Also included are a constant vorticity ring with a circular core (labelled CER in Table 1). The difference of the two initial core limit is plotted on Fig. 5 for $\sigma/R = 0.1$. The comparison of acoustic pressure signal for the two vortex ring with different initial core limit is plotted in Fig. 6. With initial circular core (CER), prior to the passage, the unsteady motion exists and the acoustic pressure is substantially larger than the Fraenkel section (FR1) with much larger signal amplitude. During the passage, the core vorticity is severely deformed and a filamentation process is induced. This triggers the high-frequency pressure emission whose characteristic period coincides with the rotation period within the two core sections. Note that due to the destabilization of the vortex core, the high-frequency emission persists even after the passage is completed for both circular and Fraenkel cores. Analysis of the computations also reveals that the high-frequency acoustic pressure emission is quadrupolar in nature [22] and consequently scales with the square of the Mach num-

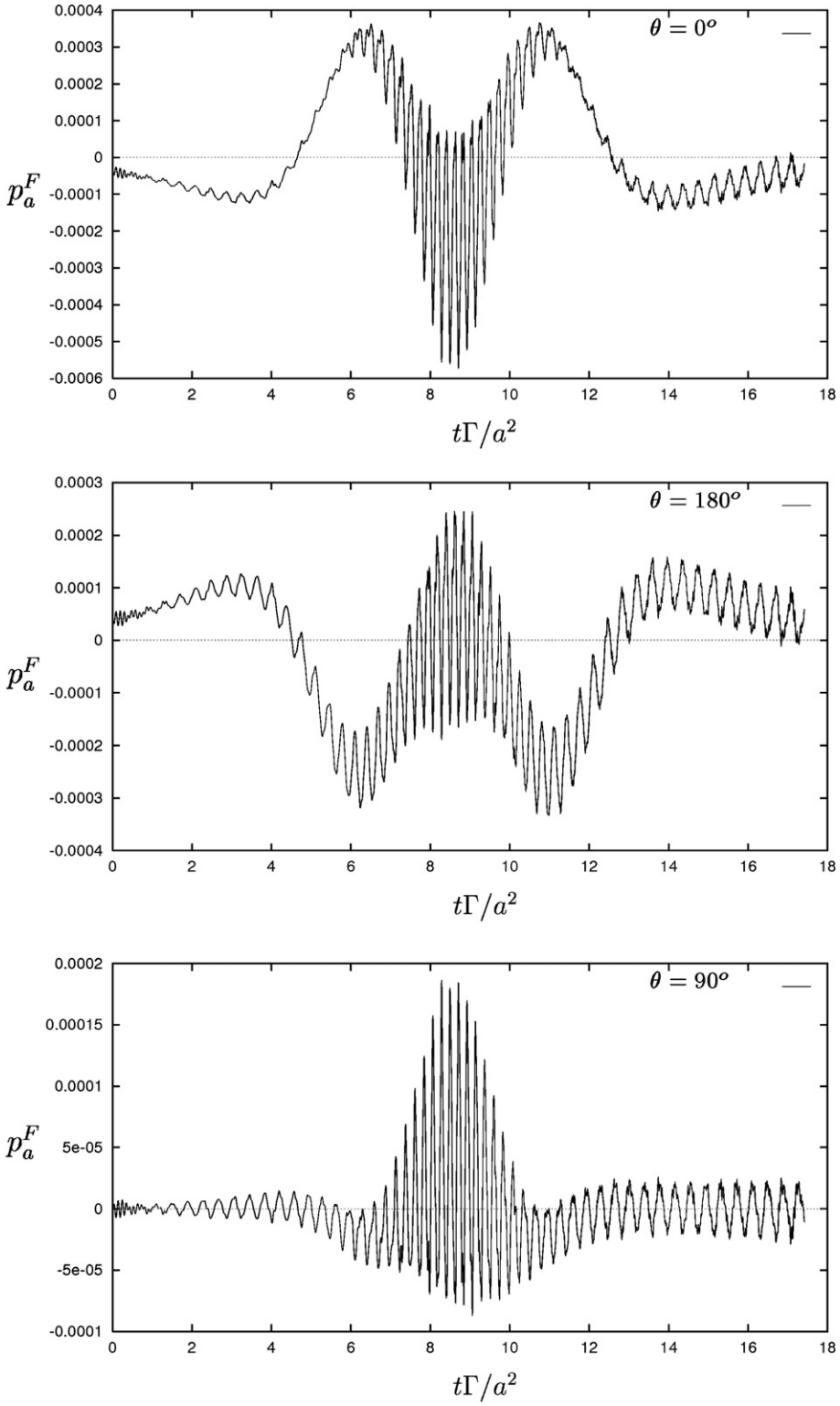

Fig. 4. Far field noise emission for the passage of a vortex ring over a sphere. The Mach number is $M = 0.05$ and the directivity is $\theta = 0^\circ$ (top), 180° (middle) and 90° (bottom). The initial ring radius is $R/a = 1$, the initial core size is $\sigma/R = 0.1$ for a constant repartition of vorticity in the section. Details the curves of Fig. 3.

Table 1
Summary of initial vortex cores used in the simulations

Core label	Core boundary ∂S in the core reference frame	Vorticity distribution within the vortex core (S)
(FR1)	$Y = \sum_{i=0}^{3} b_i \cos i\theta$ $b_0 = \mu$	$\frac{\omega_\theta}{r} = C$
(CER)	$Y = \mu$	$\frac{\omega_\theta}{r} = C$

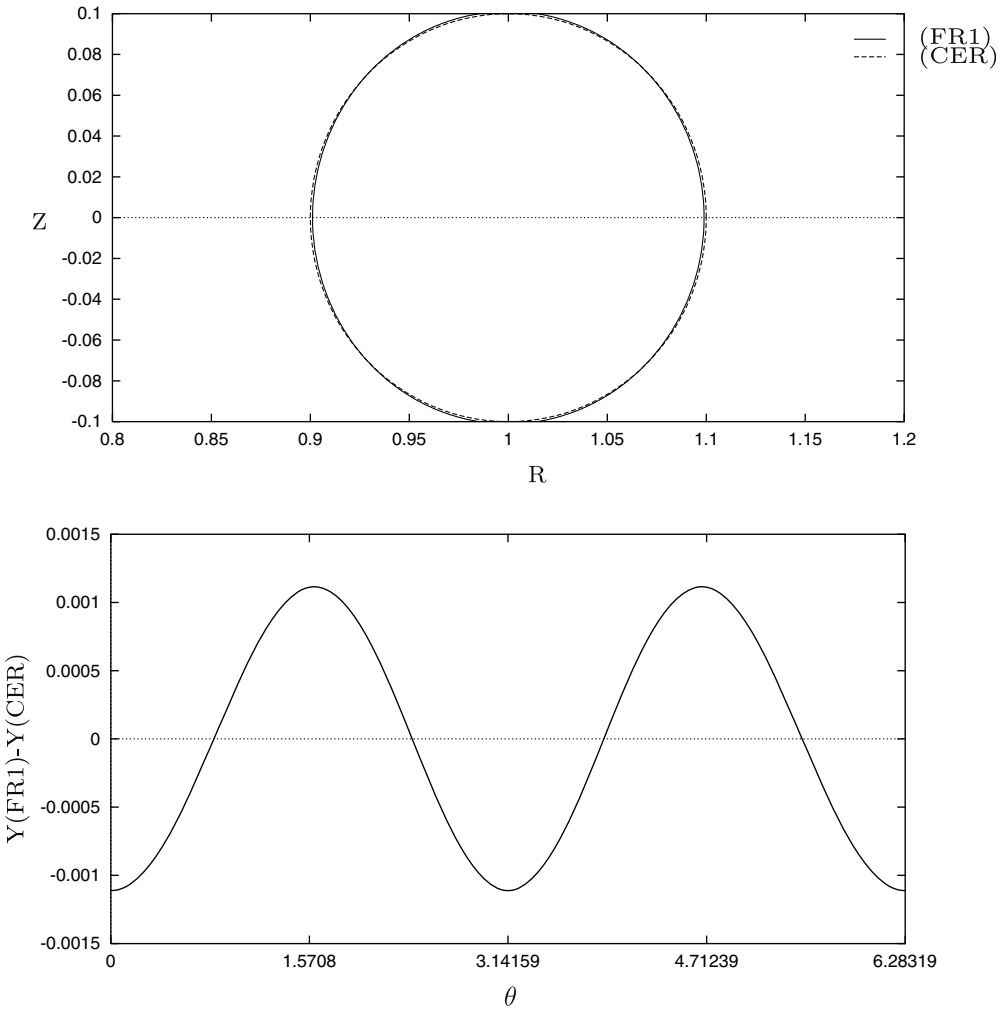

Fig. 5. Initial core limit (∂A) for a uniform distribution of vorticity in the section (top figure). Difference between the two cores limit (bottom figure), $\sigma/R = 0.1$.

ber. Meanwhile, Fig. 7 shows that when scaled by the Mach number the acoustic pressure signals along the z axis generated by the interaction with the sphere, is dominated by an $O(M)$ dipole emission.

4. Helicopter flow

From an engineering point of view, the design of helicopters calls for a wide multi-disciplinary analysis. Meaningful results can be obtained only in the context of a complete aeromechanical analysis which couples unsteady aerodynamics around the complete configuration, structural dynamics, flight mechanics and control.

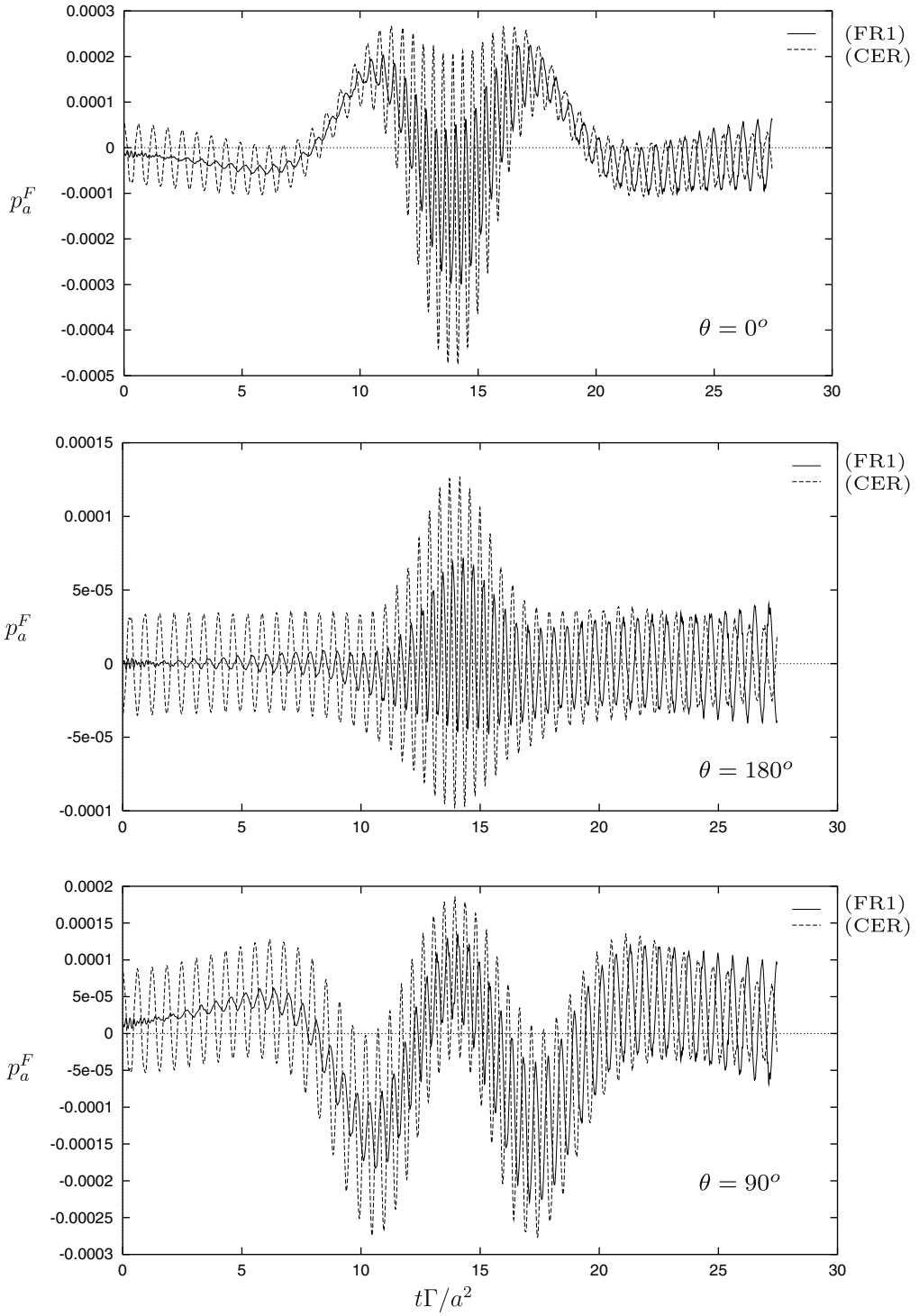

Fig. 6. Comparaison of the far field noise for two different limit core sections: CER section and FR1 section $M = 0.05$. The initial ring radius is $R/a = 1.25$, the initial core size is $\sigma/R = 0.1$ for a uniform repartition of vorticity in the section.

This is already a quite complex mixture, even before adding noise. The variety of scales both in time and space appearing in the full problem, lead to a volume of computations not affordable by current computer resources,

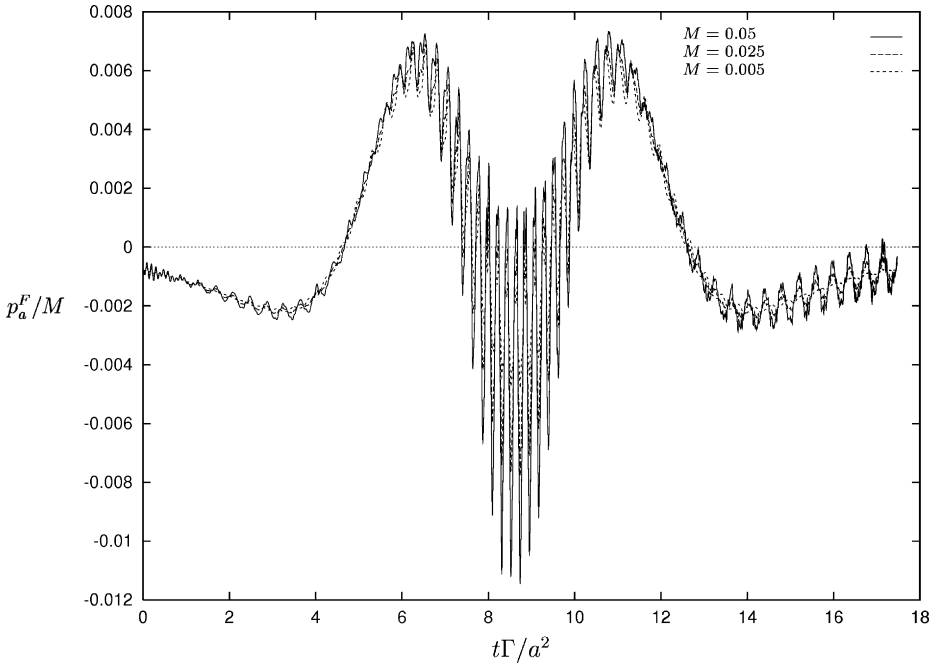

Fig. 7. Far field noise emission for the passage of a vortex ring over a sphere for different values of the Mach number M and fixed directivity $\theta = 0°$. Idem parameters than Fig. 3.

at least in engineering terms. Therefore the need for developing computationally efficient models in which acoustics can be decoupled from flow computations is both important and useful. To this end vortex methods provide such an option and the present section aims at supporting this argument.

4.1. Computational details

The results discussed next, have been obtained using GENUVP, a non-linearly coupled aeroelastic model based on the flow solver described in Section 2.2. The configuration considered includes the fuselage, the main and tail rotors MR and TR, respectively. Concerning component flexibility, the fuselage has been regarded rigid as compared to the much more flexible rotor blades. Then for the blades, their high slenderness allows to model them as beam structures. Concerning the flow assumptions, the fuselage has been considered as non-lifting body and the blades as lifting. So the model neglects the wake from the fuselage, a simplification necessary when targeting computationally efficient simulations. Otherwise one would need to solve the unsteady Navier–Stokes equations.

Solution of the complete set of equations is carried out in the time domain starting from rest. In order to avoid resolving the response of the structure to the impulsive start of the flow, first an initial flow is established assuming the structure rigid. The requirement is that the wake extends downstream of the aircraft at a distance of 2–3 MR diameters. Then the aeroelastic coupling is activated. At each step, the aerodynamic part will provide the loads on the structure while the structure will feed back the deformed geometry together with the deformation velocities. Internal iterations within each time step are needed in order to account for the non-linearities included in the equations. In the cases considered 2–3 internal loops were found sufficient.

4.1.1. The structural model

The second order beam theory developed by Hodges and Dowell [28] has been implemented [29,30]. It considers combined bending along the blade motion (lag) and in the normal direction (flap), torsion and tension in

the radial direction of the blade. Using finite element techniques the dynamic equations of an isolated blade will take the typical form:

$$[\mathbf{M}_s]\ddot{\mathbf{q}}_s + [\mathbf{C}_s]\dot{\mathbf{q}}_s + [\mathbf{K}_s]\mathbf{q}_s = \{\mathbf{F}_s\} \tag{24}$$

where $\mathbf{q}_s$ denotes the structural degrees of freedom, i.e. the displacements and rotations at the nodes of the finite element grid along the beam. Because the particular beam model is formulated with respect to the deformed state, the model is non-linear with the mass, damping and stiffness matrices $[\mathbf{M}_s]$, $[\mathbf{C}_s]$ and $[\mathbf{K}_s]$, respectively, being dependent on $\mathbf{q}_s$ and its time derivatives. Also non-linear is the expression of the loads in the right hand side of (24) which mainly contains the aerodynamic loads. The deformation velocities $\dot{\mathbf{q}}_s$ will be part of the body velocity $\mathbf{V}$ while the deformed geometry through $\mathbf{q}_s$ will modify the normal $\mathbf{n}$ both appearing in the no-penetration boundary condition for the flow. Given this, an iterative procedure is needed at every time step.

At the free end of the beam zero loading conditions are imposed while at its root (attachment point with the hub), specific kinematic conditions are needed which take into account the rigid body motions and the constraints imposed by the control system. To this end the multi-body approach is followed. It consists of extending $\mathbf{q}_s$ so as to include all of these motions. The extra equations needed are either the dynamic equations of the controller or fixed value conditions as in the case of constant rotation speed. It is noted that controls on helicopter rotors refer to rotations not necessarily small and therefore the non-linearity introduced cannot be neglected.

In all designs the pitch of the blades is constrained but often so happens for the flap and lag angle at the blade root as in hinged rotors. Controls regulate the forces and moments on the complete aircraft to specific flight requirements. So in practice, including wind tunnel tests on scaled helicopters, instead of specifying the control angles, the targeted global loads are provided also known as *trim conditions*. In simulations it is possible to automate this process by implementing simple PI controllers. During the computation, the control settings are corrected at the end of each full rotation. This point is important from a computational stand point. Starting the simulation impulsively, the initial structural response must first fade out before trimming can start. Therefore a considerable number of full rotations is required.

4.1.2. The flow model

The main concern in formulating the flow solver is its computational cost. For the type of model used, the cost depends on the paneling density and the number of vortex particles involved. Let N_p denote the number of panels on the solid boundaries, M_p denote the number of wake panels forming the wake generated within one step and N_v denote the number of vortex particles generated per time step. The cost of the potential calculations is constant and corresponds to the solution of an $(N_p + M_p)^2$ system. On the contrary the evolution of the wake will increase in time. At time step n, the particle to particle interactions needed will be $(n \cdot N_v)^2$ plus the interactions with the solid boundaries. So if a long simulation, or equivalently a large number of time steps, is required, the total cost can easily explode. Therefore it is important to take advantage of any possible cost reduction.

To this end, Vassberg's [31] idea to use tree-algorithms for solving the boundary integral equation associated to $\mathbf{u}_{solid}$, can be extended to also include dipole distributions [32], provided that piecewise constant distributions are introduced. This is clear for σ while for μ, Hess's wise choice of piecewise constant $\nabla\mu$ (or else a strictly linear μ distribution) is adopted. So the same integral evaluation is used for both the source and surface vorticity terms. This approach allows to have large number of panels which is important when dealing with complex and multi-component geometries. Note that the matrix of the corresponding system can be solved using iterative solvers of the Gauss Seidel type without requiring the storage of the full system. In the cases considered a total of 10,000 panels were used: 1000 per MR blade, 200 per TR blade and the rest on the fuselage.

Then as regards the wake calculations, the Particle-Mesh (PM) technique has been implemented [33]. It consists of substituting the direct particle-to-particle calculations in (7) by an indirect evaluation of $\mathbf{u}_\omega$ and its derivatives based on the vector potential $\mathbf{\Psi}$. To this end free vorticity $\boldsymbol{\omega}$ is projected on a cartesian grid on which $\nabla^2\mathbf{\Psi} = -\boldsymbol{\omega}$ is solved using a fast Poisson solver. Then $\mathbf{u}_\omega = \nabla \times \mathbf{\Psi}$ and its derivatives can be readily obtained on the grid nodes and subsequently back interpolated at the particle positions. For both projection and back interpolation the M_4 function given in [34] was used in all three directions.

The PM method will reduce the run time from N_p^2 to $N_p \cdot \log N_p$. The most expensive part of the PM method concerns the evaluation of $\mathbf{\Psi}$ over the boundary of the domain containing all vortex particles D_ω.

In the present implementation this part is done using the Biot–Savart law. Due to the $1/r$ behaviour of Ψ tree-algorithms can provide significant cost reduction. To this end a sequence of nested grids are introduced on D_ω. Let Δx denote the spacing of the reference grid in direction x. Then the spacing of the nested grids will be $(\Delta x)_k = 2^k \Delta x$. By projecting vorticity to each of these grids and then remesh, a sequence of particle approximations is generated $\omega_{h,k}$. Starting from the coarser grid this sequence is scanned and depending on the distance from the point of evaluation, either the computation is performed or left for the next grid level to take over. In the cases considered the sequence contained four grids plus the fine grid with size on which the PM is finally applied.

Besides the cost, in the course of a long 3D simulation, the div free condition of ω deteriorates. The PM technique offers a simple way for improving this. Instead of assuming that $\nabla \cdot \omega = 0$ in defining the vorticity stretching term, we can use $\mathrm{div}(\omega : \mathbf{u})$ [34]. This term is first calculated at the nodes of the PM grid and then interpolated to the particle positions.

Another important point is related to numerical errors. Error bounds in vortex methods are connected to particle spacing which should maintain the overlapping between the particle cores. If the computation is long, distortions will appear which will violate this requirement and therefore increase the errors. In such cases remeshing is required. Again PM techniques offer a direct and consistent way to do remeshing. Instead of retaining the original positions of the vortex particles, a new set of particles is defined by integrating the vorticity at the nodes of the grids.

Although the PM method has high potential in reducing the computational cost, the user can still end up having shortage of computer resources. The good performance of the PM method is directly linked to the use of fast Poisson solvers which require uniform grid spacing in two of the three space directions. Therefore for a given space resolution (typically less that 0.01 of the MR diameter D), the size of the PM grid is proportional to the length of the wake and therefore the total duration of the simulation. In the cases considered the wake extended over a length in the order of 10 MR diameters. Of course the same grid resolution is not required over the entire wake. So D_ω is split into subdomains (Fig. 8) which are subsequently considered separately. To this end boundary conditions will be needed also over the interfaces of the subdomains indicated as thick lines. For the interface contained in the shaded area of Fig. 8, the contribution of particles not belonging to it is calculated using tree based direct Biot–Savart computation while for the rest a local PM solution is carried out. For helicopters one can distinguish two main subdomains: the near region containing the aircraft and the far region which covers the rest which can be further split if needed. High resolution is needed in the near region while further downstream coarser resolutions are acceptable. In the near region, the presence of solid boundaries on which the computation of the velocity is needed, but cannot fit into a cartesian grid, requires special treatment. Particles close to boundaries are excluded from the PM computations and their contribution on the solid boundaries is added at the end using the Biot–Savart law.

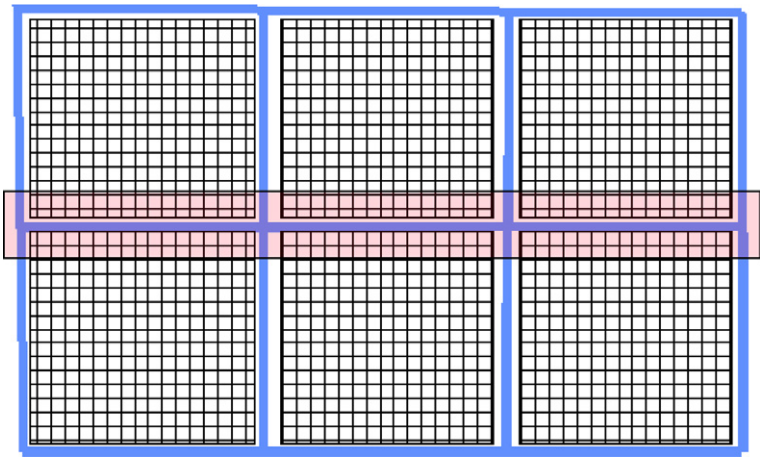

Fig. 8. Schematic view of the domain decomposition for the PM implementation.

The next point is linked to remeshing which offers a means to maintain the accuracy of the computation. In the cases considered D_ω is not densely populated with particles. There are holes in space which we have to respect otherwise remeshing can easily generate a prohibitively high number of particles. To this end it is important to introduce a strategy that activates remeshing wherever beneficial. Fortunately, by referencing the particles to grid nodes makes such a search and decision procedure local and therefore affordable.

The next point concerns the defining assumptions of vortex methods. In their original formulation, vortex methods are both incompressible and inviscid. This is certainly a drawback. Although viscous solvers have been successfully incorporated into the toolbox of vortex methods [35], they are expensive and hence opposite to the target of keeping the cost low. Fortunately, in many aerodynamic flows it is possible to approximately include these effects. For high *Re* number flows, viscous effects can be introduced as boundary layer corrections. Anticipating the obvious objection that this is an old fashioned approach, it is noted that the current state of art in helicopter aeroelasticity is based on look-up tables and semi-empiric dynamic inflow models, so including boundary layer corrections is not that bad. In fact in the absence of shock waves strong viscous–inviscid interaction models provide satisfactory predictions even in dynamic stall [36]. On rotors, a low cost approach consists of applying viscous corrections in a section by section procedure based on the 3D inviscid surface velocity field. The method is a modification of the 2D model described in [36]. Instead of considering the section isolated as in the original model, the contribution of the other blade sections is added as an additional external field.

We can also add efficiently compressibility effects in a similar way by either solving the full potential equations [37] or the 2D Euler equations on a section-by-section basis [32]. This part requires sectional grids which however will be restricted to only the outer part of the blade and therefore the extra cost is affordable. The 3D calculation provides the inflow conditions to the grid – only the in plane to the section velocity components are included. In doing so the contribution of the section under consideration in the 3D flow field should be excluded.

Helicopter noise is closely related to BVI. The simulation in this respect is approximating the trajectory of particles approaching a solid surface. If the smaller local scales are not taken into account, it is possible that particles cross the boundary. Besides violating the boundary condition, in many cases the simulation blows up. In order to prevent such crossings, an approximate local scheme was devised in [38]. It consists of locally solving the trajectory equations based on the continuity equation and the already known flow velocity on the boundary and at the starting particle location.

The last point concerns the output of the flow solver. In addition to the flow velocity which is a direct output, the surface loading is also needed. Loading mainly consists of the pressure distribution. In the baseline model, the pressure field is obtained as the sum of a potential term calculated by means of the Bernoulli equation and a vortical part calculated by solving the following Poisson equation: $\nabla^2 p = -\rho\nabla(\boldsymbol{\omega}\times\mathbf{u})$ with the source term defined exclusively at the particle locations [39]. In case boundary layer corrections are added, then the same procedure is still valid provided that the corrected velocity is used. As additional output the drag force is obtained which is needed as input to the structural solver.

4.1.3. The acoustic model

Retaining the monopole and dipole terms in (1), integration in the context of generalized functions has led Farassat [15] to the following, so called formulation 1A, which provides the acoustic pressure $p(\mathbf{x},t)$ in the following form:

$$\begin{aligned}4\pi p(\mathbf{x},t) = &\int_S \left[\frac{\rho_o(\dot{V}_n + V_{\dot{n}})}{r(1-M_r)^2}\right]_{\text{ret}} \mathrm{d}S(y) + \int_S \left[\frac{\rho_o V_n(r\dot{M}_r + c(M_r - M^2))}{r^2(1-M_r)^3}\right]_{\text{ret}} \mathrm{d}S(y)\\ &+\frac{1}{c}\int_S \left[\frac{\dot{l}_r}{r(1-M_r)^2}\right]_{\text{ret}} \mathrm{d}S(y) + \int_S \left[\frac{l_r - l_M}{r^2(1-M_r)^2}\right]_{\text{ret}} \mathrm{d}S(y)\\ &+\frac{1}{c}\int_S \left[\frac{l_r(r\dot{M}_r + c(M_r - M^2))}{r^2(1-M_r)^3}\right]_{\text{ret}} \mathrm{d}S(y)\end{aligned} \tag{25}$$

Integration is performed over a moving surface S with velocity $\mathbf{V}$ and unit normal $\mathbf{n}$. S usually coincides with the collection of all solid boundaries but it can be any closed surface containing all noise sources as in the case of important quadrupole terms [16]. In the former, $\mathbf{V}$ will include the rigid as well as the deformation velocity components while the flow parameters are introduced through the local Mach vector $\mathbf{M} = \mathbf{u}/c$ and the loading distribution $\mathbf{l}$. Both sets of data are included in the output of the aeroelastic simulation. All calculations are done in the retarded (emission) time $\tau = t - f(r)/c$ where $f(r)$ depends on the distance $\mathbf{r}$ between the emission point $\mathbf{y}$ and the receiver $\mathbf{x}$ as well as on the conditions at infinity [19]. Otherwise in (25), the dot denotes time derivative, $V_n = \mathbf{V}\cdot\mathbf{n}$, $V_{\dot{n}} = \mathbf{V}\cdot\dot{\mathbf{n}}$, $M_r = \mathbf{M}\cdot\mathbf{r}/r$, $l_r = \mathbf{l}\cdot\mathbf{r}/r$, $l_M = \mathbf{l}\cdot\mathbf{M}$.

Because the source information: the surface velocity and the loading, is provided in the emission time, the arrival time at the receiver will be source specific. So in order to reconstruct the total sound pressure signal at a receiver position, the separate signals are interpolated in time. In order to achieve better resolution, both the grid and the time stepping for the sources can be finer than that of the flow solver. Such a refinement will affect the calculation of the arrival time and not the content of the primitive flow variables which have been evaluated for specific space and time resolution. Otherwise the acoustic calculation will reproduce the quality of the flow computations. In this connection, the time step plays the major role. In helicopter applications, by expressing the time step as azimuth increment, a step of at least 2° turns out to be necessary.

4.2. Results

The described model has been evaluated against wind tunnel measurements within the recently concluded HeliNoVi project [40] and presented in [41–43]. The wind tunnel tests were conducted on a 1:2.5 scaled model of the BO105 helicopter in the open section of the *German Dutch Wind Tunel* (DNW) in different flight conditions (Fig. 9). The 4 m diameter four bladed MR is hingeless and pitch controlled. The pitch angle θ is defined with respect to the azimuth position of each blade ψ by the collective θ_0 and cyclic θ_c, θ_s angles: $\theta(\psi) = \theta_0 + \theta_c\cos(\psi) + \theta_s\sin(\psi)$. The 1.7 m diameter two bladed TR is teetering at an angle of 45° providing passive pitch–flap coupling. The control system regulates the thrust of the TR by imposing the collective pitch angle θ_{TR}. Both rotors rotate at constant speeds with adjustable ratio. In order to facilitate validation, the speed ratio was set equal to 5. The database of the campaign includes recordings of: the unsteady pressures on the blades of both rotors, the loads along the MR blades and at the hub and the acoustic signals around aircraft. In certain flight conditions the inflow over both rotors has been recorded using particle image velocimetry (PIV) as well as the elastic deformations at the tip of the MR using stereo pattern recognition (SPR). So this database offers a significant opportunity to validate aeroelastic and aeroacoustic simulations over a wide range of flight conditions.

We start with the flow characteristics of the simulations. In Fig. 10, the azimuth variation of the normal to the chord aerodynamic force coefficient CN at $r/R = 0.87$ of the MR is shown for a 6° descent flight at 33 m/s (left) and a level flight at 60 m/s. The agreement is satisfactory especially in descent flight. The BVI encounters which are known to be the main drive of noise in this type of flight, are well captured both in terms of position and amplitude. In level flight, the overall agreement is good, however over the first and forth quadrants there are differences. In the advancing side of the blade motion (first quadrant), the flight velocity will increase the local (relative) Mach number and therefore compressibility effects become important. When a section-by-sec-

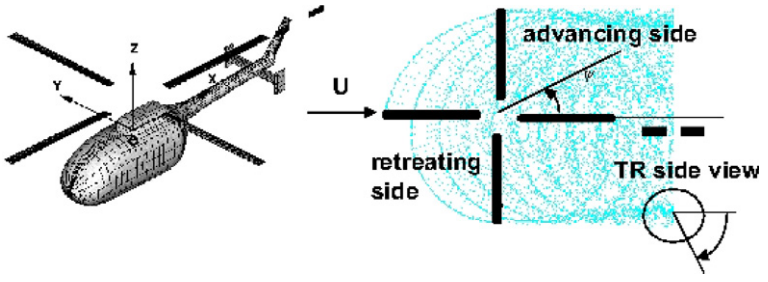

Fig. 9. Layout of the BO105.

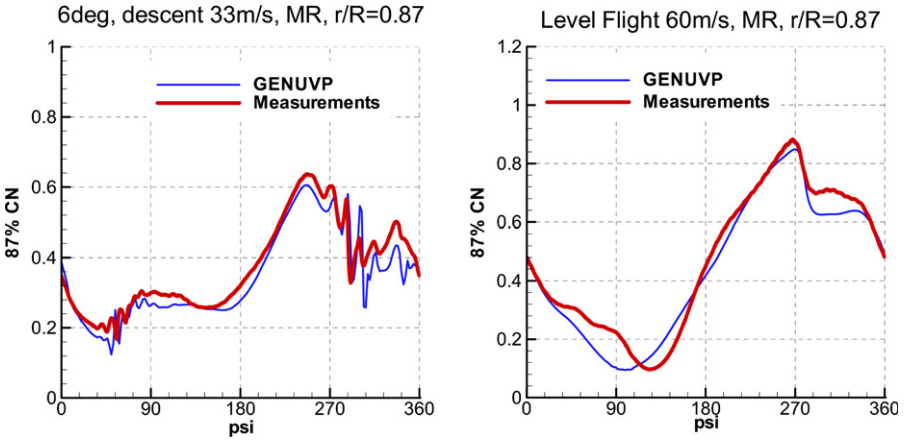

Fig. 10. Azimuth variation of the normal to the chord aerodynamic force coefficient at $r/R = 0.87$ of the main rotor in 6° descent flight at 33 m/s (left) and in forward flight at 60 m/s (right).

tion 2D compressible Euler correction is applied the predictions are improved. In Fig. 11, the pressure distributions at the same section are shown for two azimuth positions. At $\psi = 90°$ the shock is properly predicted while at $\psi = 45°$ there is an early onset of the shock. At 90° the flow is approximately 2D while at 45° the inflow will have an important radial component which can explain part of the difference suggesting the use of a 3D Euler solver. Although this is true, it is important to note that there exist several possible sources of error other than the modelling assumptions. The entire simulation depends on trimming the rotors. Any deviation in the structural properties of the system will affect the computed control angles and through them all derived quantities will be affected.

Returning to the descent flight case, a better view of the BVI encounters is given in Fig. 12 in which the azimuth variation of the pressure fluctuations at points close to the leading edge are compared to measurements. The particular choice of sensors is justified by the fact that the NACA23212 section of the blade is front loaded and therefore important noise sources are expected in the leading edge region. Besides a slight underprediction of the amplitudes, the correlation with measurements is good. BVI is regulated by the relative position and motion of the blade with respect to the over passing vortices. As the blade is flexible the quality of predictions in this respect are connected to the structural part of the simulation. They will also depend on the computed flow velocity that convects vortices. Relevant measurements in this particular case were not conducted, so we switch to a forward flight case at 50 m/s for which tip deformations and flow field measurements

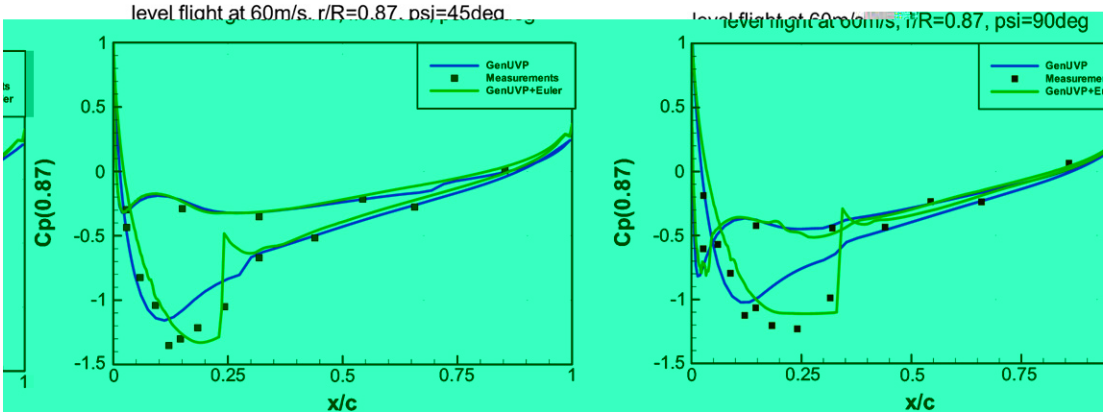

Fig. 11. Instantaneous pressure distributions at $r/R = 0.87$ of the main rotor in forward flight at azimuth locations $\psi = 45°$ and 90°. Measurements are compared with baseline predictions (GENUVP) and predictions based on 2D Euler computations (GENUVP + Euler).

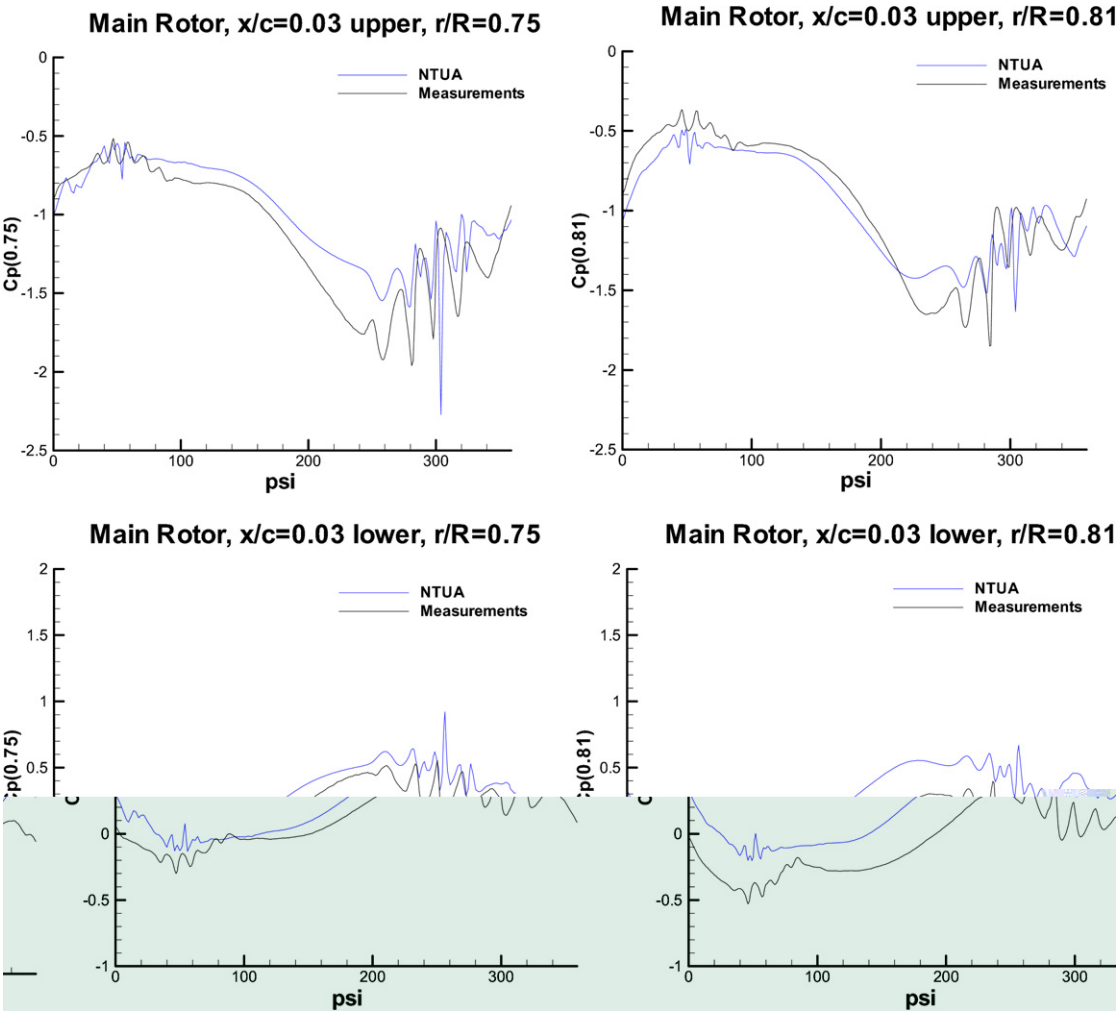

Fig. 12. Pressure time series at the leading edge ($x/c = 0.03$) of the MR blade over a full rotation during a 6° descent flight. Results at the upper (suction) side of the blade are on top while results at the pressure side are beneath. The columns correspond to radial locations $r/R = 0.75$ and 0.81, respectively.

are available. In Fig. 13, a snapshot of the computed normal to the MR disk velocity w distribution over the retreating side is compared to PIV measured data. In both figures the computed blade and the tip vortex positions are added in order to facilitate the discussion. Besides a small azimuth phase shift, there is close correlation. The locations of the tip vortices are well predicted although with more concise cores as expected. Also the normal to the rotor disk w velocity distribution which modulates the rotor thrust, is well predicted.

Next with respect to blade deformations, results are shown in Fig. 14 for the same case. The frequency content of the elastic response of the blade will contain the rotational frequency of the MR also referred as 1/rev and its harmonics. The level and the 1/rev variation of the flap deformation is well predicted. There is a phase shift in the predictions as well as a small underestimation of the 3/rev response. With respect to the lag deformation, the higher harmonic is predicted but with a smaller amplitude. There is a level shift which is attributed to some measurement discrepancy (the measurements are constantly positive). Finally, as regards the torsion, the 1/rev is dominant over the 3/rev. The predictions indicate a phase shift while they fail to produce the 3/rev in accordance with the flap predictions. To some extent these differences have been attributed to the structural input data and possibly to the hub dynamics which due to lack of data was assumed rigid (Ref. [43]).

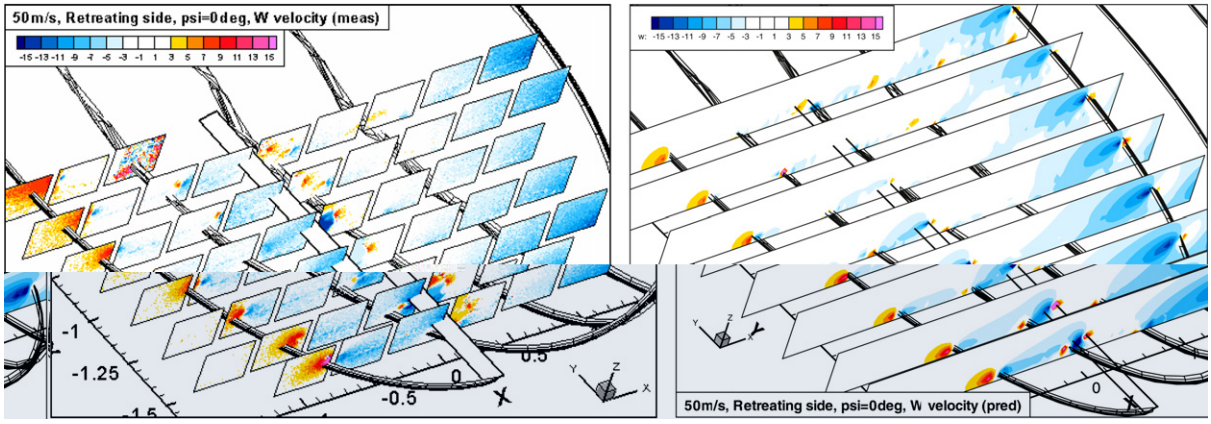

Fig. 13. Snapshot of the normal to the MR disk velocity component over the retreating side in forward flight at 50.9 m/s. Meaurements are on the left and predictions on the right.

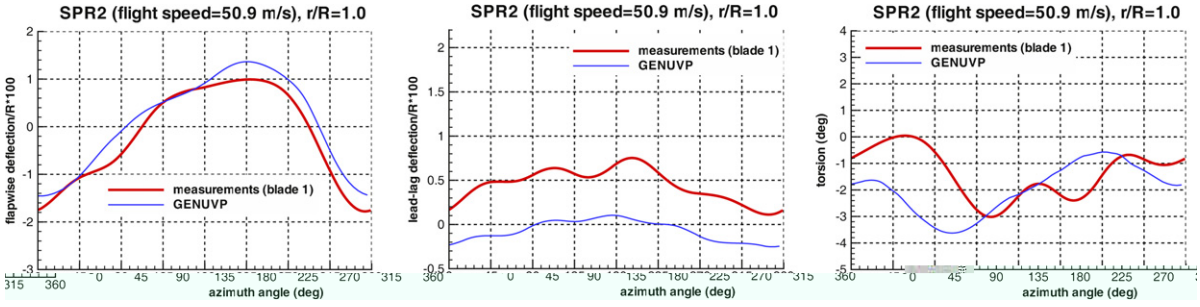

Fig. 14. Deformations at the tip of the MR blade in forward flight at 50.9 m/s.

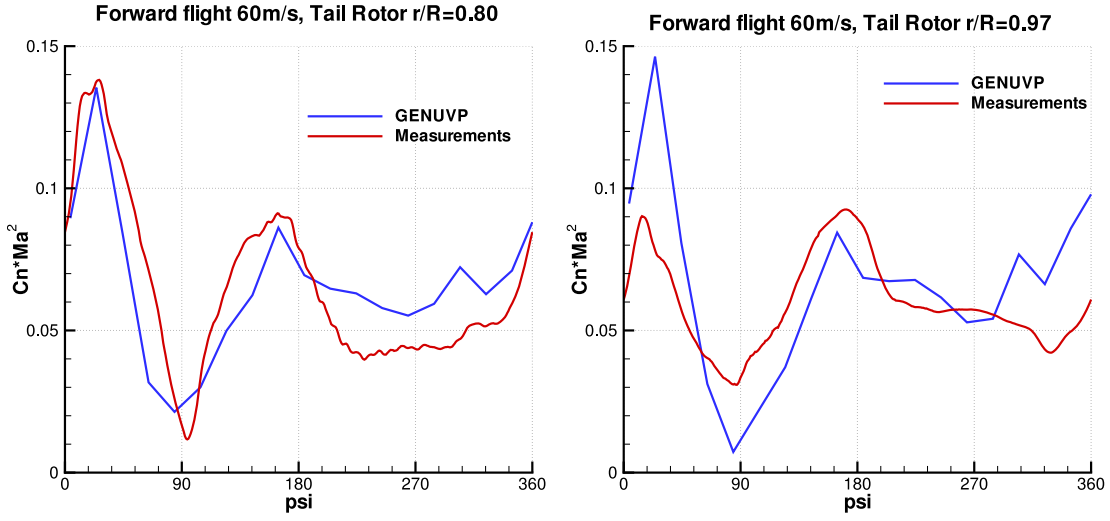

Fig. 15. Azimuth variation of the normal to the chord force coefficient at $r/R = 0.80$ and 0.97 of the tail rotor in forward flight at 60 m/s.

Also the TR contributes to noise becoming dominant in forward flight as a result of its operation in the wake of the MR. The TR rotates five times as fast as the MR. Thus, even if the time step is reduced at the level of 1° azimuth step for the MR, the resolution in the TR is just acceptable. In Fig. 15, the azimuth var-

iation of the normal to the chord force coefficient is compared to measurements at $r/R = 0.8$ and 0.97. Despite the complexity of the incoming flow to the TR and the relatively low resolution, the model especially at $r/R = 0.8$ compares well with the measurements. In both plots two peaks appear both due to BVI with the MR tip vortices. At $r/R = 0.97$, the first peak is over-predicted. Using PIV the flow on the two sides of the TR was measured allowing to calculate the out of plane vorticity component. In Fig. 16, the predicted and measured vorticity fields are compared. The approaching MR tip vortex is well captured. The MR vortex is almost normal to the TR plane and because of that the passage of the TR blade keeps it intact. This event corresponds to the second peak in Fig. 15 at $\psi \simeq 180°$. The first peak at $\psi \simeq 20°$ takes place after the MR vortex has passed the tail fin. Over the plane of TR inflow located between the TR and the tail fin, the flow

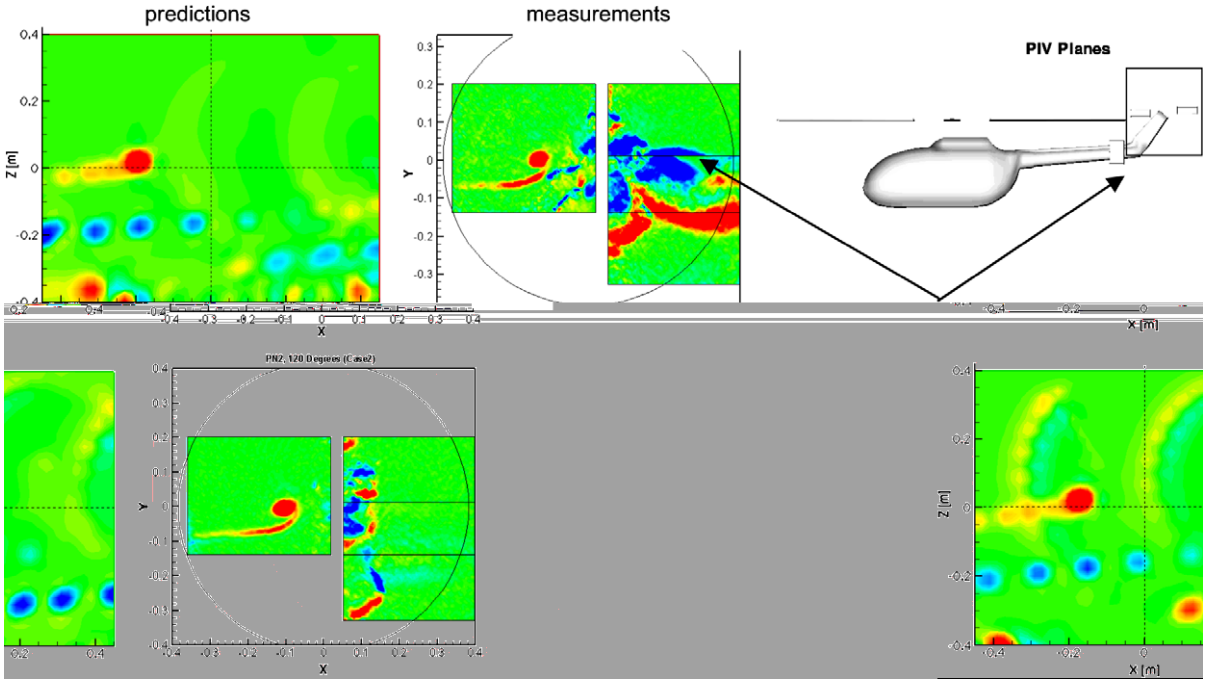

Fig. 16. Vorticity contours at planes on both sides of the TR in forward flight at 60 m/s. Upper row corresponds to the inflow plane and lower row to the outflow plane. Predictions are on the left while measurements on the right.

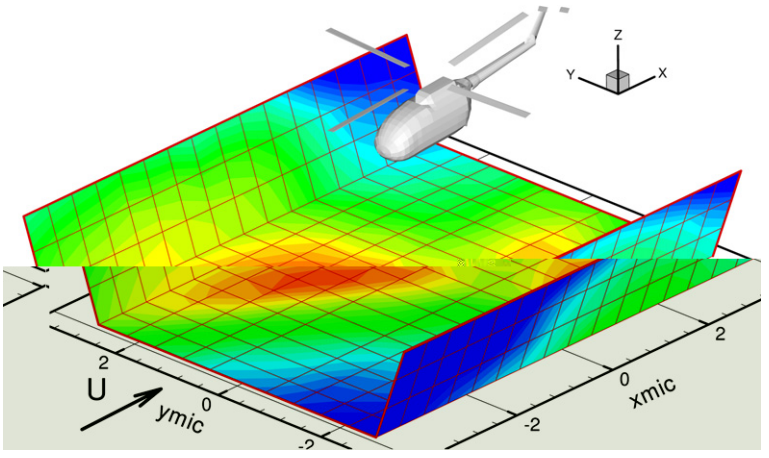

Fig. 17. Positions of the microphones.

appears distorted in the measurements. This could be due to the wake of the tail fin. It is expected to feed the TR plane with wake vorticity which is lost after the passage of the TR blade as a result of mixing. Addition-

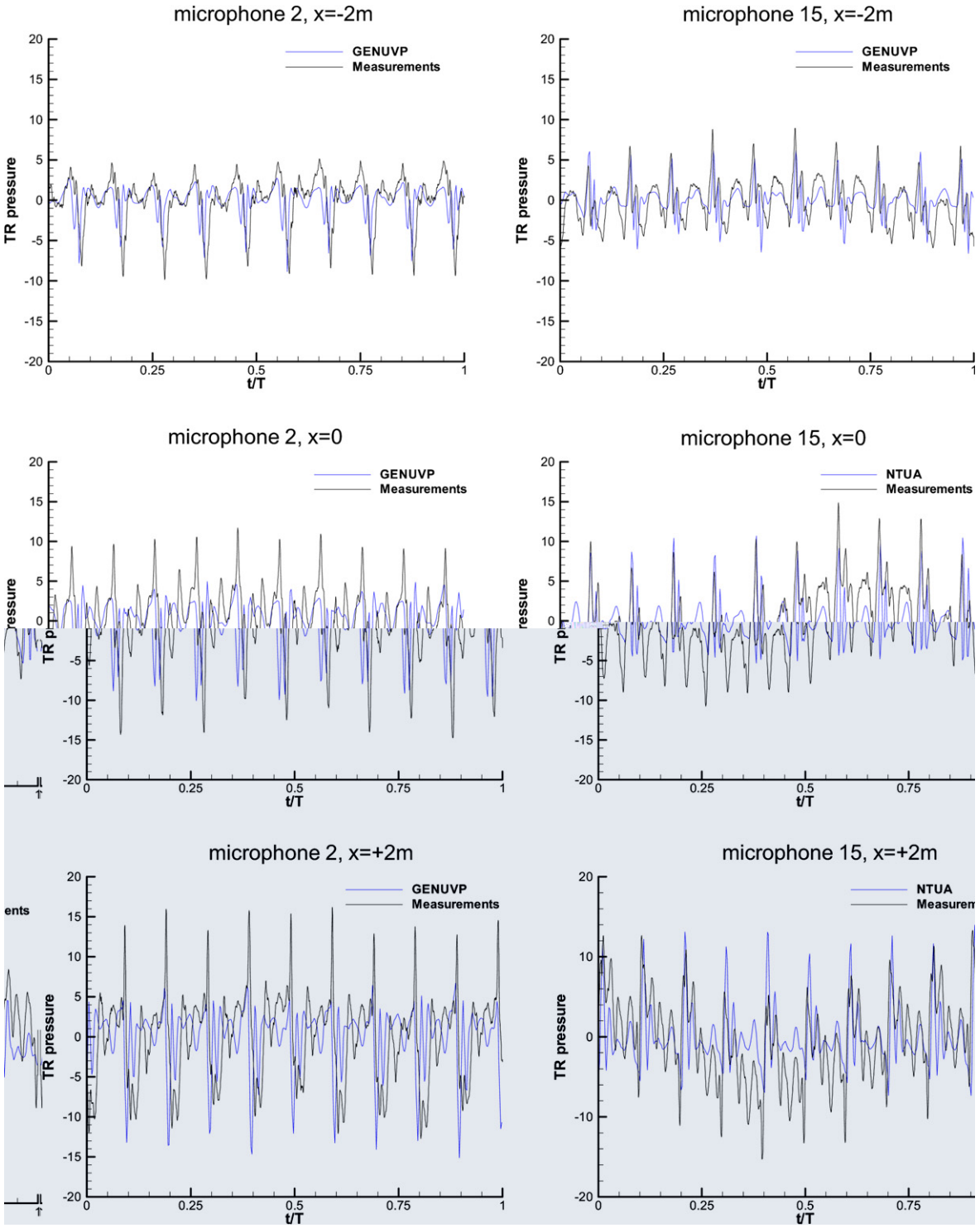

Fig. 18. Acoustic pressure distributions. The columns correspond to the two sides of the TR disk while the rows correspond to different streamwise locations, the center of the rotor being at $x = y = 0$.

ally, it is possible that reflections of the light sheet on the tail further distort the pictures. In the simulation the wake of the tail fin is not modelled so there is no mixing and therefore the MR tip vortex hits the blade in full

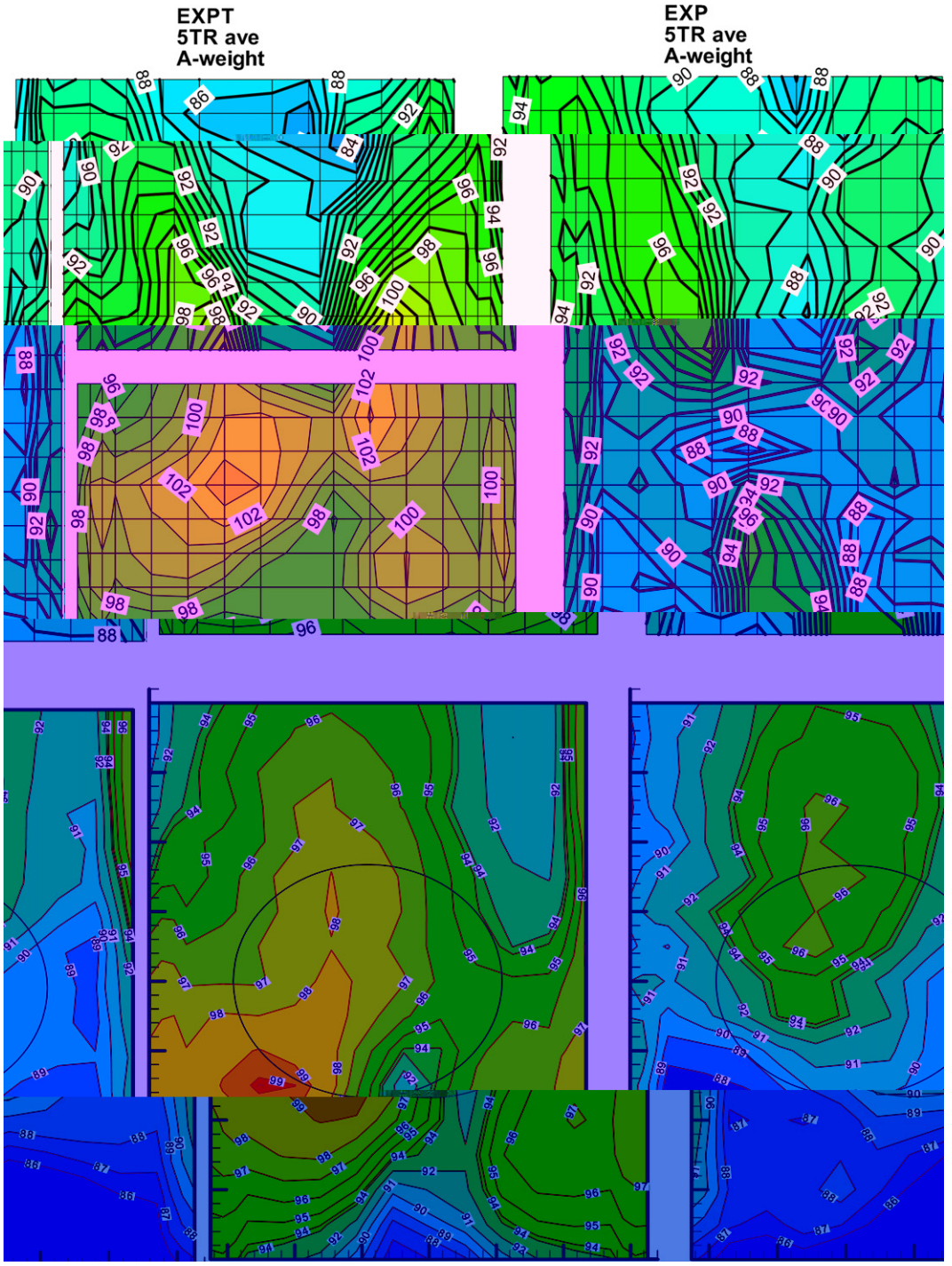

Fig. 19. A weighted noise level contours in case of forward flight at 60 m/s. In the upper row measurements averaged over five TR rotations (5TR ave) are shown while predictions are in the lower row. Left column corresponds to operation with the TR rotating with its advancing side down (EXPT) while right column corresponds to the same flight conditions but with the sense of rotation of the TR opposite (EXP).

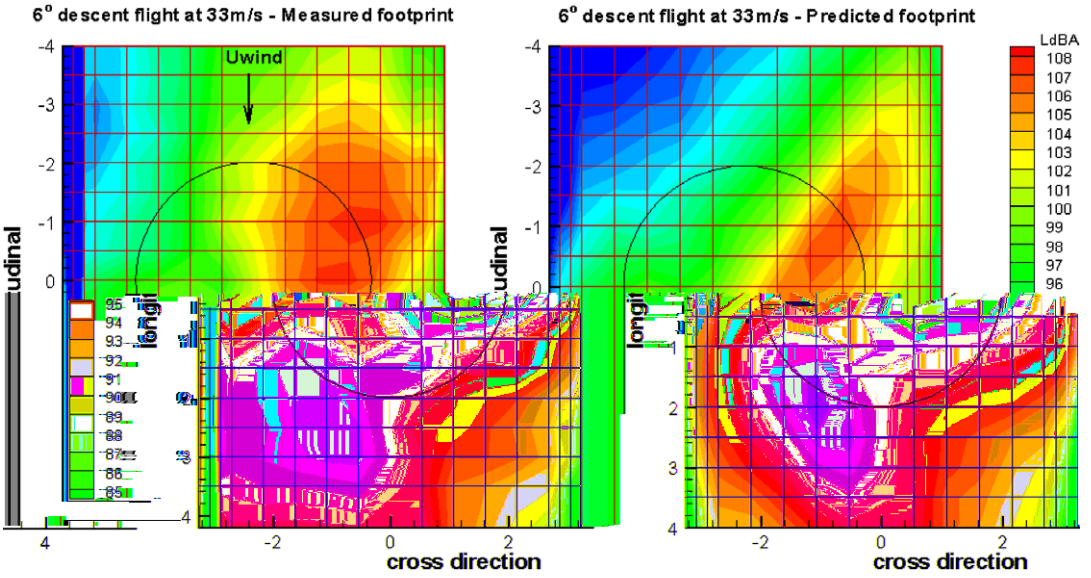

Fig. 20. Noise level contours in case of 6° descent flight at 33 m/s.

strength. This could explain the over-prediction of the first peak at $r/R = 0.97$ in Fig. 15. Note that it is the tip section that first hits the MR vortex so larger differences are expected at $r/R = 0.97$ compared to those at $r/R = 0.8$. Another point concerns the dynamics of the TR hub which will affect the position of the TR in space which due to teetering will be self-adjusted. Specific details were not provided so the hub was regarded rigid which can also introduce deviations. In any case the differences are small considering the complexity in the TR region.

Next acoustic results are shown. Evaluation of predictions is carried in terms of acoustic signals and noise contours (noise footprint) which is mostly used in practice. In Fig. 17, the nodes of the grid denotes the positions of the microphones. For given x they are numbered from 1 to 16 following the positive y direction. Fist the forward flight case is considered in view of analysing the noise contribution of the TR. In Fig. 18, six signals are presented which correspond to receivers located at the two sides of the TR disk (Fig. 17). There is good correlation with the measured data except for some phase shift which can be easily connected to drifts in the ratio of the rotation speeds of the two rotors finally achieved during the tests. It is noted that deviations from an integer value of this ratio cannot be tackled by simulations as it would lead to an exceedingly high number of rotations in order to achieve periodicity. Next in Fig. 19 noise contours are presented in two cases both in forward flight at 60 m/s. They differ in the sense of rotation of the TR. They concern one of the potential way to reduce noise as simulations indicated already prior to the test which finally confirmed that a significant reduction can be achieved. By reversing the sense of rotation, the MR vortices will inpinge the TR blades while retreating resulting less pronounced pressure fluctuations. Of course part of the reduction is related to the fact that the advancing side which contributes significantly to the overall noise level is brought to a longer distance from the receivers but even if this effect is substracted there is still significant reduction. Finally, as regards the descent flight case which is known to be the noisiest condition, comparison of predicted and measured footprints is given in Fig. 20. The most noisy regions are well predicted both in terms of position and size with an over-prediction of the maximum level of approximately 1 dB.

5. Conclusions

The usage of the vortex particle method as the flow solver providing the necessary input for noise calculations has been considered. In the case non-linear compressibility effects are either negligible or localised, results indicate that satisfactory predictions can be obtained under relatively low cost. In this respect it is reconfirmed that the vortex particle method is a powerful tool which besides being cost effective, has no dif-

ficulty to adopt in a multi-disciplinary context as defined for realistic full helicopter configurations. The application of the particle method to the case of a helicopter in forward and descent flight including within one single code aeroelasticity and aeroacoustic modelling is believed to provide a demonstration of this. Although it results from a complex combination of a lot of sophisticated techniques together with empirical simplifications, it is probable that the particle method will still have a long life in numerical modelisation of complex flows. Every step forward of the usual Navier–Stokes solver will probably corresponds to a step forward of the particle method in the accounting of more complex configurations.

For a part, this ability of particle methods to provide such results, relies on two particular properties: first, the particle method is able to solve a transport equation with a very low diffusion error, even when a re-gridding procedure has to be activated, second they are based on integral formulations which naturally include an exact account of external boundary conditions. As a result, the particle method interest is extended to the ability of producing very detailed and even very accurate solutions to problems for which vorticity conservation and non-reflecting boundary conditions are of paramount importance; noise prediction is actually one of them.

Acknowledgement

Part of this work has been financed at NTUA by the European Commission under Contract G4RD1-CT-2002-00667 (HeliNOVI: Helicopter Noise and Vibration Reduction).

References

[1] A. Chorin, Numerical study of slightly viscous flow, J. Fluid Mech. 57 (4) (1973) 785–796.
[2] A. Leonard, Vortex methods for flow simulation, J. Comput. Phys. 37 (1980).
[3] L. Greengard, V. Rokhlin, A Fast Algorithm for Particle Simulations, J. Comput. Phys. 73 (1987) 325–348.
[4] B. Couet, O. Buneman, A. Leonard, Simulation of three-dimensional incompressible flows with a vortex in cell method, J. Comput. Phys. 39 (1981) 305–328.
[5] G.S. Winckelmans, J.K. Salmon, M.S. Warren, A. Leonard, The fast solution of three-dimensional fluid dynamical *N*-body problems using parallel tree codes: vortex element method and boundary element method, in: Proceedings of the Seventh SIAM Conference on Parallel Processing for Scientific Computing, Philadelphia, SIAM, 1995, pp. 301–306.
[6] P. Koumoutsakos, A. Leonard, F. Pépin, Boundary conditions for viscous vortex methods, J. Comput. Phys. 113 (1) (1994) 52–61.
[7] J. Lighthill, Waves in Fluids, Cambridge University Press, 1978, 520 pp..
[8] M. Nitsche, J.H. Strickland, Extension of the gridless vortex method into the compressible flow regime, J. Turbul. 3 (2002), (Art. No. 001).
[9] J.D. Eldredge, T. Colonius, A. Leonard, A vortex particle method for two-dimensional compressible flow, J. Comput. Phys. 179 (2) (2002) 371–399.
[10] J.D. Eldredge, The dynamics and acoustics of viscous two-dimensional leapfrogging vortices, J. Sound Vib. 301 (2007) 74–92.
[11] C. Rehbach, Numerical calculation of three-dimensional unsteady flows with vortex sheets, La Recherche Aerospatiale (1977) 289–298.
[12] B. Cantaloube, S. Huberson, A new approach. Using vortex point method for prediction of rotor performance in hover and forward flight, Vertica 2 (1986) 4360.
[13] J.E. Ffowcs Williams, D.L. Hawkings, Sound generation by turbulence and surfaces in arbitrary motion,Philos. Trans. R. Soc. Lond. A 342 (1969) 264–321.
[14] D.G. Crighton, A.P. Dowling, J.E. Ffowcs Williams, M. Heckl, F.G. Leppington, Modern Methods in Analytical Acoustics, Springer-Verlag, 1992.
[15] K.S. Brentner, F. Farassat, Modeling aerodynamically generated sound of helicopter rotors, Prog. Aerosp. Sci. 39 (2–3) (2003) 83–120.
[16] P. Di Francescantonio, A new boundary integral formulation for the prediction of sound radiation, J. Sound Vib. 202 (4) (1997) 491–509.
[17] J.L. Hess, Calculation of potential flow about arbitrary three-dimensional lifting bodies, McDonnell Douglas Rep. MDC J5679-01, 1972.
[18] S. Voutsinas, Vortex methods in aeronautics: how to make things work, Int. J. Comput. Fluid Dynam. 20 (1) (2006).
[19] J. Prieur, G. Rahier, Aeroacoustic integral methods, formulation and efficient numerical implementation, Aerosp. Sci. Technol. 5 (2001) 457–468.
[20] O.M. Knio, L. Ting, R. Klein, Interaction of a slender vortex with a rigid sphere: dynamics and far-field sound, J. Acoust. Soc. Am. 103 (1998) 83.
[21] R. Klein, O.M. Knio, L. Ting, Representation of core dynamics in slender vortex simulations, Phys. Fluids 8 (1996) 2415.

[22] E. Rivoalen, S. Huberson, O.M. Knio, Numerical study of sound radiation by axisymmetric vortex rings, J. Comput. Acoust. 11 (1) (2003) 11–45.
[23] H. Lamb, Hydrodynamics, Cambridge University Press, 1992.
[24] M. Nitsche, R. Krasny, A numerical study of vortex ring formation at the edge of circular tube, J. Fluid Mech. 276 (1994) 139–161.
[25] E. Rivoalen, S. Huberson, Numerical simulation of axisymmetric viscous flows by means of a particle method, J. Comput. Phys. 152 (1999) 1–31.
[26] E. Rivoalen, S. Huberson, O.M. Knio, Sound generation by the interaction of a vortex ring with a rigid sphere, in: Vortex Flows and Related Numerical Methods III, ESAIM, Proceedings, vol. 7, 1999.
[27] L.E. Fraenkel, On steady vortex rings of small cross-section in an ideal fluid, J. Fluid Mech. 51 (1972) 119–135.
[28] D.H. Hodges, E.H. Dowell, Nonlinear equations of motion for elastic bending and torsion of twisted non-uniform blades, NASA TN D-7818, 1975.
[29] S. Voutsinas, V. Riziotis, Structural dynamics of wind turbines, in: J.-F. Brouckaert (Ed.), Wind Turbine Aerodynamics: A State of the Art, VKI Lectures Series 2007-05, 2007.
[30] S. Voutsinas, Report on pre-test aeroelastic calculations, D2.1-3 HeliNoVi Report, 2003.
[31] J.C. Vassberg, A fast surface panel method capable of solving million-element problems, AIAA Paper 97-0168, 1997.
[32] S. Voutsinas, D. Triantos, High resolution aerodynamic analysis of full helicopter configurations, in: Proceedings of the 25th European Rotorcraft Forum, Rome, Paper C-11, 1999.
[33] J. Christiansen, Numerical simulation of hydrodynamics by the method of point vortices, J. Comput. Phys. 13 (1973) 363–379.
[34] G-H. Cottet, P.D. Koumoutsakos, Vortex Methods: Theory and Practice, Cambridge University Press, 2000.
[35] P. Koumoutsakos, A. Leonard, High resolution simulations of the flow around an impulsively started cylinder using vortex methods, J. Fluid Mech. 296 (1995) 1–38.
[36] V. Riziotis, S. Voutsinas, A viscous–inviscid interaction model for dynamic stall simulations on airfoils, Int. J. Numer. Methods Fluids 56 (2008) 185–208.
[37] M.H.L. Hounjet, J.-C. LeBalleur, D. Blaise, G. Bernandini, A. Pisoni, Maturation of a full potential based rotor flow field code, in: Proceedings of the 26th European Rotorcraft Forum, The Hague, The Netherlands, September 2000.
[38] S. Huberson, Etude asymptotique et numérique de nappes tourbillonnaires enroulées, Thèse de l'Université Pierre et Marie Curie, 1986.
[39] A. Mangin, Expérimentations numériques sur les phénomèmes tourbillonnaires, Thèse de l'Université Pierre et Marie Curie, 1990.
[40] H.-J. Langer, O. Dieterich, S. Oerlemans, O. Schneider, B. Van der Wall, J. Yin, The EU HeliNoVi Project – wind tunnel investigations for noise and vibration reduction, in: Proceedings of the 31st European Rotorcraft Forum, Florence, Italy, 2005.
[41] A. Visingardi, A. Dummel, D. Falchero, M. Pidd, S. Voutsinas, J. Yin, Aerodynamic interference in full helicopter configurations: validation using the HeliNoVi database, in: Proceedings of the 32nd European Rotorcraft Forum, Maastricht, The Netherlands, 2006.
[42] M. Pidd, A. Dummel, D. Falchero, A. Visingardi, S. Voutsinas, J. Yin, Assessment noise emission from full helicopter configurations: validation using the HeliNOVI database, in: Proceedings of the 32nd European Rotorcraft Forum, Maastricht, The Netherlands, 2006.
[43] O. Dieterich, H.-J. Langer, O. Schneider, G. Imbert, M.H.L. Hounjet, V. Riziotis, I. Carafelli, R. Calvo Alonso, C. Clerc, K. Pengel, HeliNOVI: current vibration research activities, in: Proceedings of the 31st European Rotorcraft Forum, Florence, Italy, 2005.